A Search For Dark Matter in the Monojet + Missing Transverse Energy Signature in 6.7 fb^{-1}

S.Z. Shalhout, T. Schwarz, R. Erbacher, J. Conway
On Behalf of the CDF Collaboration
http://www-cdf.fnal.gov

P. Fox, R. Harnik
Fermilab
http://www.fnal.gov

Y. Bai
SLAC
http://www.slac.stanford.edu

(Dated: November 23, 2011)

We present the results of a search for dark matter production in the monojet + missing transverse energy signature. We analyze a sample of Tevatron $p\overline{p}$ collisions at $\sqrt{s}$=1.96 TeV, recorded by the CDF II detector, and corresponding to an integrated luminosity of 6.7 fb^{-1}. In events with significant missing transverse energy and one energetic jet, we find good agreement between the standard-model backgrounds and the observed data. We consider three modes of dark matter production: axial-vector mediated, vector mediated, and t-channel mediator exchange. In each mode, the mediator couples to standard-model quarks and dark matter, where the dark matter is a Dirac fermion. We set 90% credibility level upper limits on 42 model points with varied values of mediator and dark matter mass between 0.96 and 42.8 pb. The limits are translated into bounds on nucleon-dark matter scattering rates.

Preliminary Results

I. INTRODUCTION

Cosmological evidence strongly indicates that baryonic matter comprises less than 20% of the total matter content of the universe [1]. In contrast, direct-detection experiments, which aim to detect dark matter-nucleon scattering, have yielded potentially contradictory null and positive results [2], with several experiments reporting signals suggestive of low-mass (~ 10 GeV) WIMP dark matter [3–5]. In collaboration with the author's of Ref. [6], we report the results of a search for dark matter in the monojet + missing transverse signature, utilizing a CDF data sample corresponding to an integrated luminosity of 6.7 fb^{-1}. We study events with significant missing transverse energy and one energetic jet, and extract 90% credibility level (CL) upper limits on the value of $\sigma(p\bar{p} \rightarrow \chi\bar{\chi} + \text{jet})$, where χ is a dark matter particle and the jet originates from initial state radiation.

In [6–9], the results of previous collider searches [10–12] in the monojet + missing transverse signature, are reinterpreted in the context of dark matter searches, with extrapolations of the collider results into limits on the dark matter - nucleon scattering rate yielding strong bounds for low-mass dark matter, spin-dependent interactions, and heavy mediators. Here, we consider models in which χ is a Dirac fermion, and where dark matter production is mediated by a massive state $\mathcal{M}$, which couples to χ and standard-model quarks. We set bounds on the production of dark matter with mass between 1 and 300 GeV, in models of axial-vector mediated, vector mediated, and t-channel mediator exchange, which we denote as A-V, V, and T respectively.

We probe matter-dark matter interactions that are relevant for direct-detection searches. In direct-detection experiments, scattering rates are described by an effective theory containing only dark matter in addition to standard-model fields. As the momentum transfer in dark matter scattering is far lower than the mass of the particle mediating the interaction, effective theory provides a valid description.

In the first set of models we analyze here, we assume that the effective theory is also valid at collider scales. This assumption is appropriate if the mediator's mass is above several hundred GeV. To capture a variety of phenomena we will study three such theories, introducing the following operators [6, 7] :

$$\mathcal{O}_V = \frac{(\bar{\chi}\gamma^\mu\chi)(\bar{q}\gamma_\mu q)}{\Lambda^2} \quad (1)$$

$$\mathcal{O}_{A-V} = \frac{(\bar{\chi}\gamma^\mu\gamma_5\chi)(\bar{q}\gamma_\mu\gamma_5 q)}{\Lambda^2} \quad (2)$$

$$\mathcal{O}_T = \frac{(\bar{\chi}P_L q)(\bar{q}P_R\chi)}{\Lambda^2} + L \leftrightarrow R\,. \quad (3)$$

We assume a universal sum of these operators over all quark flavors. The operator $\mathcal{O}_V$ can be induced by integrating out a heavy vector particle which interacts both with a pair of quarks and with a pair of dark matter particles. The operator $\mathcal{O}_{A-V}$ may be induced by a similar particle with purely axial-vector coupling, while $\mathcal{O}_T$ would be induced by a set of heavy colors scalars (such as a squarks). In direct-detection experiments the vector operator leads to spin-independent dark matter scattering, while the axial-vector is spin-dependent. The t-channel operator includes both spin-dependent and independent terms, but in practice the latter will dominate due to the coherent nature of spin-independent scattering.

To constrain these effective theories we implement very heavy mediators, well above the Tevatron reach (at 10 TeV), which couple to quarks and dark matter as described above in MadGraph [13]. With these models we derive efficiencies well within the effective field theory regime, and place limits on the cross section at the Tevatron. These bounds can be translated to bounds on Λ and to direct-detection limits.

In a collider environment, with large momentum transfers, the effective theory approach is not necessarily valid [6, 7, 14]. This may change the limits on dark matter, in particular, in the limit in which the mediators are very light. Far below the typical p_T [15] at the Tevatron, it has been shown that collider limits are completely relaxed [6, 7, 14]. In order to explore this possibility and how it affects our limits we consider models in which the mediators are not far from the characteristic scale at the Tevatron. We thus consider mediators with a mass of 100 GeV and a width of 10 GeV for the vector and axial-vector cases. For the t-channel case we consider a mediator mass of 400 TeV and a width of 8 GeV [16]. The Tevatron limits on the dark matter-production cross section place bounds on the couplings of mediators with these fixed masses, which are presented as direct-detection limits.

The analysis can be summarized as follows : we select events with one jet of transverse energy, E_T, above 60 GeV, and missing transverse energy, $\not\!\!E_T$ [17], above 60 GeV, and allow for up to one additional jet with $20 < E_T < 30$ GeV. We impose several selections, including a multivariate rejection, to reduce the large backgrounds from multijet QCD processes. We define several 'control regions' used to validate the data-model, and expect a contribution of $53,904 \pm 6,022$ events from background processes in our 'signal-region' selection. This compares well to our observed total of 52,633 events. We compute 90% credibility level upper limits on $\sigma(p\bar{p} \rightarrow \chi\bar{\chi} + \text{jet})$ using the binned lead-jet E_T for data, model components, and signals. Following [6, 8], we convert our limits into bounds on the dark matter nucleon scattering rate for both spin-dependent (σ_{SD-p}) and spin-independent (σ_{SI-p}) interactions.

This note describes the details of the search and is structured as follows: Section II describes the initial (trigger) online event selection and the data sample considered. Section III details the selections used to identify a sample of candidate events consistent with the expected topology of the $p\bar{p} \to \chi\bar{\chi} + \text{jet}$ process, and defines the various control regions used for modeling cross-checks. The composition of our selected sample, simulation of the signal samples, and the formulation of our data model are discussed in Section IV. Section V contains a discussion of the systematic uncertainties, and results are presented in Section VI.

II. DATA SAMPLE & ONLINE EVENT SELECTION

The data used in this search were collected by the upgraded CDF II detector, between February 2002 and June of 2010, and correspond to 6.7 fb^{-1} of Tevatron $p\bar{p}$ collisions at $\sqrt{s}$=1.96 TeV. The CDF II detector is described in detail elsewhere [18] and consists of tracking systems immersed in a 1.4 T magnetic field, surrounded by calorimetery providing coverage for $|\eta| < 3.6$. A system of drift chambers external to the calorimetery provides muon detection capability for $|\eta| < 1.5$.

CDF II records only those collision events that meet the criteria of a three-level online event-selection (trigger) system. In this search, we use data selected by any of several variants of a $\not\!\!E_T$ trigger algorithm, which require $\not\!\!E_T > 40$ GeV. In combination the $\not\!\!E_T$ triggers have a selection efficiency of approximately 90% (95%) for events with $\not\!\!E_T \sim 70$ GeV (≥ 90 GeV).

III. CONTROL & SIGNAL REGION SELECTIONS

The sample of events meeting the requirements of the $\not\!\!E_T$ trigger are subject to four categories of selections denoted PreSelection, EWK Control, QCD Control and Signal Region. The events passing EWK and Signal Region selections are maintained as exclusive categories, while the events passing QCD Control selections are a subset of those passing PreSelection. The PreSelection consists of requirements designed to reject poorly reconstructed events, events from non-collision sources, and events with fake $\not\!\!E_T$. The QCD control selections are designed to preferentially select events arising from multijet processes, while the EWK selection favors Z and W boson processes through the requirement that events contain at least one isolated track [19] of $p_T > 10$ GeV/c. The Signal Region selections identify the sample of events used in the extraction of upper limits on the dark matter production rate.

The full PreSelection requirements are: The data was to have been recorded with fully-functioning calorimeter and muon systems. The primary interaction vertex is required to be well-centered [20] within the CDF detector, and the maximum separation between any two vertices must be less than 90 cm. The $\not\!\!E_T > 60$ GeV, and the lead-E_T jet [21] has $E_T > 35$ GeV and $|\eta| < 1.0$. The event does not contain a cosmic ray track or calorimeter activity that is out-of-time with $p\bar{p}$ bunch crossings [22]. The event EM fraction [23] is between 0.35 and 0.85, and the $\not\!\!E_T$ significance [24] is less than 15. There are no jets in regions of poor or incomplete calorimeter coverage and no jets with an EM fraction greater than 0.9. The magnitude of the TrkMET_{10} [25] is required to be less than the $\not\!\!E_T$ to reject events with track mis-reconstruction.

The QCD Control Region selections are: Events are required to pass the PreSelection. The lead-E_T jet has $E_T > 60$ GeV, and is required to contain at least one track [19] of $p_T > 10$ GeV/c within the jet. The event does not contain an isolated track with $p_T > 10$ GeV/c. In order to enhance the multijet content of this selection, we require events to **fail** one or more of the following selections : $NN_{QCD} > 0.3$ (defined below) **OR**, the event only has 1 or 2 jets with $E_T > 20$ GeV **OR**, the second jet has $E_T < 30$ GeV **OR** , $\Delta\Phi(\vec{\not\!\!E}_T, \text{lead-}E_T \text{ jet}) > 2.5$ **OR**, $\Delta\Phi(\vec{\not\!\!E}_T, \text{TrkMET}_{10}) < 0.4$ **OR**, the minimum $\Delta\Phi(\vec{\not\!\!E}_T, \text{any jet}) < 0.4$.

The EWK Control Region and Signal Region selections are nearly-identical, differing only in that events are required (for EWK) or forbidden (for Signal) to contain an isolated track $p_T > 10$ GeV/c. Both selections have the following requirements in common : Events must meet the PreSelection requirements (they are however as noted above, maintained as exclusive samples). The lead-E_T jet has $E_T > 60$ GeV, and is required to contain at least one track [19] of $p_T > 10$ GeV/c within the jet. The $NN_{QCD} > 0.3$, and the event only has 1 or 2 jets with $E_T > 20$ GeV. If there is a second jet, it has $E_T < 30$ GeV. The $\Delta\Phi(\vec{\not\!\!E}_T, \text{lead-}E_T \text{ jet}) > 2.5$, and $\Delta\Phi(\vec{\not\!\!E}_T, \text{TrkMET}_{10}) < 0.4$, and the minimum $\Delta\Phi(\vec{\not\!\!E}_T, \text{any jet}) < 0.4$.

NN_{QCD} Inputs
minimum $\Delta\Phi(\vec{\not\!\!E}_T$,any jet)
R [27]
$\Delta\Phi(\vec{\not\!\!E}_T$,lead-$E_T$ jet)
$\not\!\!E_T$
Lead-jet E_T
Number of jets
$\Delta\Phi(\vec{\not\!\!E}_T$,TrkMET$_{10}$)
Magnitude of the TrkMET$_{10}$
$\Delta\Phi$(TrkMET$_{10}$, lead-E_T jet)
Event EM fraction
Lead-jet detector η

TABLE I: Distributions input to the NN_{QCD}.

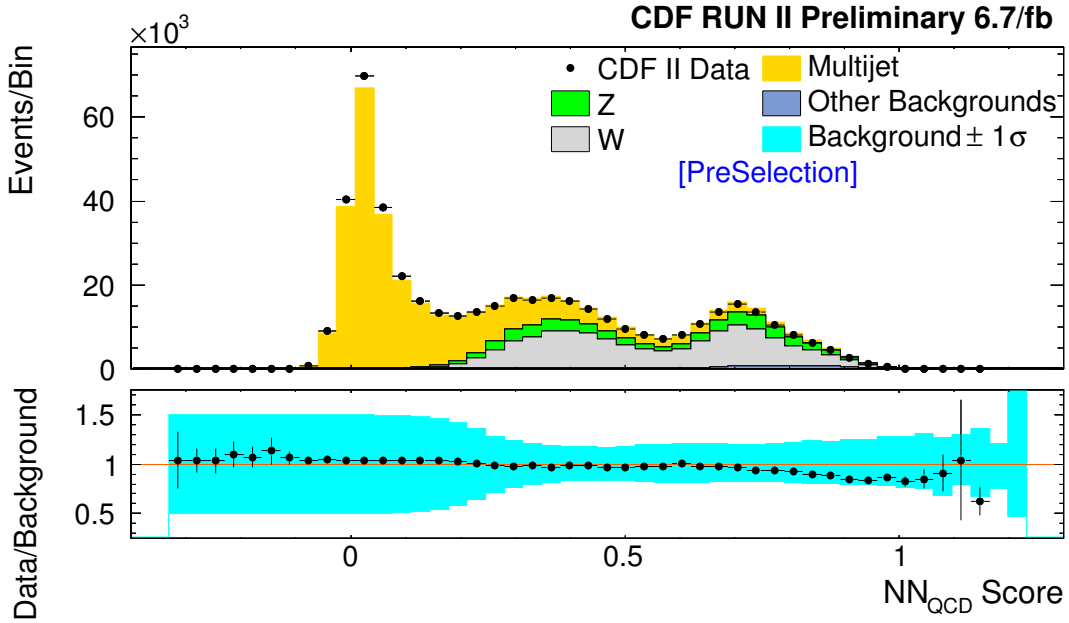

FIG. 1: NN_{QCD} output for PreSelection data and simulated processes. We reject events with $NN_{QCD} < 0.3$.

A. Multijet Rejection with an Artificial Neural Network

Multijet events (here, primarily QCD dijet with minor contributions from γ+jet) enter the monojet + $\not\!\!E_T$ selection whenever jets are mis-reconstructed or lost. These backgrounds are particularly significant at high jet E_T, have large uncertainties, and would diminish sensitivity to a dark matter signal. In order to effectively reduce the contribution of multijet processes to our signal region, we employ an artificial neural network (NN_{QCD}) designed to isolate multijet events. The NN_{QCD} was trained to separate PreSelection data from a combination of simulated Z, W, $t\bar{t}$, single-top, and diboson processes. The NN_{QCD} is a Multilayer Perceptron (MLP) implemented in TMVA [26], trained on 140,000 data and 140,000 simulated events. The NN_{QCD} has 12 hidden nodes in a single layer and 11 input nodes corresponding to the input distributions listed in Table I. To enter the Signal Region, an event must return a NN_{QCD} score greater than 0.3. We find that this requirement eliminates ∼83% of multijet events, and maintains a ∼90% efficiency for dark matter samples. The network output for events passing PreSelection is shown in Figure 1.

Parameter	binning
Magnitude of TrkMET_{10}	[0,1,10,20, $\geq$ 200]
Minimum $\Delta\Phi(\vec{\not\!\!E}_T$,any jet)	[0,0.5,0.8,2,3,3.1,3.14]
Number of Jets	[1,2,$\geq$ 3]
$\not\!\!E_T$	[60,70,$\geq$ 200]
$\not\!\!E_T$ significance	[0,7.5,15.1]
R	[0,0.45,0.5,0.55,1]

TABLE II: Parameters and binning forming the multijet rate matrix.

IV. DATA MODEL

We model contributions from Z and W boson processes using ALPGEN [28] with PYTHIA [29] for particle showering and hadronization. Signal, diboson (ZZ, WZ, WW), and $t\bar{t}$ processes are modeled with PYTHIA. Single-top contributions are modeled using MADGRAPH [13] with PYTHIA for showering. The simulations assume a top mass of 172.5 GeV. The detector response is modeled using a detailed GEANT-based detector simulation [30].

The normalization of ALPGEN samples is determined by the leading-order ALPGEN predictions, with an additional K-factor of 1.4 for Z boson and 1.36 for W boson processes. The top-samples are normalized assuming cross sections of 7.4, 1.05, and 2.1 pb for $t\bar{t}$, s-channel single-top, and t-channel single top respectively, while diboson normalizations assume production rates of 11.34 (WW), 3.47 (WZ), and 3.62 (ZZ) pb [31]. All simulated samples utilize CTEQ5L [32] parton distribution functions (p.d.f's). We correct the luminosity profile of simulated samples to match that observed in data, and adjust the normalization to compensate for small ($\sim 1\%$) differences in the $|Z_0| < 60$ cm [20] efficiency observed between data and simulated samples. We parameterize [33] the efficiency of the trigger selection in $\not\!\!E_T$, and apply an additional weight to each simulated event to reflect the likelihood of trigger selection.

A. Multijet Model

Events originating in multijet processes enter the monojet + $\not\!\!E_T$ selection primarily due to misconstruction or mis-measurement of the energy of one or more jets. This makes simulation of the multijet contribution to our selected samples difficult (in simulated QCD dijet samples the acceptance was found to be $<< 1\%$). Instead, we rely on a 'data-derived' model, utilizing the well-established rate matrix approach [34].

In the application of the rate matrix method to this search, we parameterize the probability that an event arises from a multijet process as :

$$\mathcal{P}_{MJ} = \frac{\text{Number of Observed Data Events} - \text{Total Prediction of Simulated Model Components}}{\text{Number of Observed Data Events}} \tag{4}$$

To estimate the shape of the multijet component of a given sample of events, each event is weighted by $\mathcal{P}_{MJ}$. $\mathcal{P}_{MJ}$ is formed as a six-dimensional histogram, with the content of each bin set by Equation 4. The six parameters forming the rate matrix and the binning utilized are shown in Table II.

The rate matrix is populated using events in the PreSelection Region. Since the QCD Control region is a subset of the PreSelection Region, both the PreSelection and QCD regions are utilized for closure (or self-consistency) tests of the rate matrix's performance. In addition, the EWK control region provides an exclusive sample for the validation of the multijet prediction.

As described in [34], the rate matrix does not necessarily predict the normalization of the multijet background with any accuracy. To form a properly normalized model, we perform fits of the model (allowing the multijet normalization to float) to the data in the PreSelection, QCD and EWK selections. We determine the Signal Region multijet normalization in a 'side-band' fit using events with $0.2 \leq NN_{QCD} \leq 0.3$ and passing all other Signal Region selections. The normalization factors are listed in Table III. To cover the observed differences in the resulting normalization factors, we assign a 50% uncertainty on the multijet normalization.

The rate matrix predicts a multijet contribution only in bins with an observed data event. This feature results in a dependence of the multijet prediction on the distribution of observed events. To reduce this limitation, we replace the matrix prediction for the multijet component of the Signal Region lead-jet E_T shape, with a template derived from a probability distribution function (PDF). The PDF is set by fitting a double-Gaussian distribution to the matrix's multijet prediction. A random sampling of the PDF is then used to populate the lead-jet E_T template used in the extraction of limits on the dark matter rate.

Selection	Scale Factor
PreSelection	0.98
QCD Control	1
EWK Control	1.38
Signal Region	0.58

TABLE III: Normalization scale factors applied to the multijet rate matrix's prediction. We assign a 50% uncertainty on the scale factors.

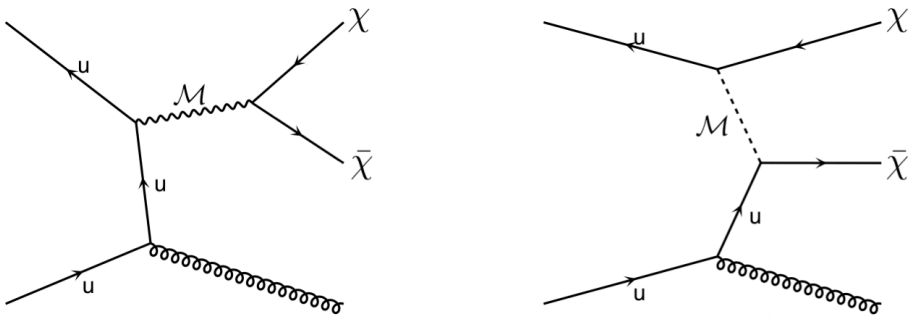

FIG. 2: Representative diagrams for dark matter production. (left) Diagram for vector or axial-vector mediated dark matter (χ) production. (right) A t-channel mediator ($\mathcal{M}$) exchange.

B. Non-Collision Model

To estimate the potential contribution from non-collision processes we utilize events identified by specialized CDF algorithms designed to isolate events arising from non-collision sources [22]. The algorithms identify events containing cosmic ray tracks, out-of-time energy, and events with low electromagnetic or track activity [22] with an efficiency of 99%. To model remaining contamination, we normalize a sample of algorithm-identified non-collision events to 1% of their initial number, and include this sample as an additional component of our background model. We assign a 100% rate uncertainty on the normalization of this background, and in addition, we assign a 1% normalization uncertainty on all simulated backgrounds, to account for the observed over-rejection rate of the algorithms in these samples.

C. Signal Models

We simulate 42 models of dark matter production using MadGraph [13] with Pythia for showering. Representative diagrams for signal processes are shown in Figure 2. Table IV details the model points and displays the predicted production rate.

$M_{\mathcal{M}}$ (GeV)	M_{χ} (GeV)	model	cross section (pb)	eff. (%)	model	cross section (pb)	eff. (%)	model	cross section (pb)	eff. (%)
10000	1	A-V	1.81e-05	2.42	T	3.03e-06	2.55	V	1.81e-05	2.44
10000	5	A-V	1.81e-05	2.46	T	3.04e-06	2.59	V	1.82e-05	2.46
10000	10	A-V	1.77e-05	2.51	T	3.01e-06	2.59	V	1.82e-05	2.48
10000	50	A-V	1.29e-05	2.76	T	2.41e-06	2.88	V	1.61e-05	2.61
10000	100	A-V	7.44e-06	2.99	T	1.59e-06	3.13	V	1.19e-05	2.86
10000	200	A-V	1.89e-06	3.17	T	5.42e-07	3.35	V	4.76e-06	3.13
10000	300	A-V	3.52e-07	3.13	T	1.37e-07	3.38	V	1.32e-06	3.17
100	1	A-V	4393.36	1.28	T	0.62	3.09	V	4396.13	1.28
100	5	A-V	4319.04	1.30	T	0.62	3.11	V	4393.98	1.29
100	10	A-V	4099.17	1.29	T	0.61	3.14	V	4384.08	1.29
100	50	A-V	154.58	1.63	T	0.43	3.58	V	977.08	1.46
100	100	A-V	4.56	2.62	T	0.24	3.99	V	14.08	2.48
100	200	A-V	0.16	3.16	T	0.06	4.33	V	0.63	3.07
100	300	A-V	0.01	3.27	T	0.01	3.87	V	0.05	3.19

TABLE IV: Signal models and Signal Region selection efficiency. The cross sections are obtained from MadGraph.

V. SYSTEMATICS

The following uncertainties are assigned on the normalization of all simulated background components. We assume a 3.8% uncertainty on the integrated luminosity due to uncertainty on the inelastic $p\bar{p}$ cross section. An additional (uncorrelated) uncertainty on the integrated luminosity is assigned to account for uncertainties specific to the CDF II luminosity monitor. We include a 1% uncertainty to account for the uncertainty in the measurements of the $|Z_0| < 60$ cm efficiency correction factors, a 2% uncertainty on the parameterization of the $\not\!\!E_T$ trigger efficiency, and a 1% uncertainty to account for the over-efficiency of non-collision rejection.

We apply an 8% uncertainty on the normalization of W and Z boson samples following [35]. Similarly, we assume uncertainties of 6% and 10% for diboson and top processes, respectively, following [31]. We estimate the effect of Q^2 uncertainties on the normalization of Alpgen-modeled samples by varying the choice of renormalization scale; we find a small change in acceptance and assign a 2% normalization uncertainty on Z and W processes to account for this effect. We include a systematic on the normalization of simulated samples to account for p.d.f. uncertainties [36]. We estimate a 1.4% uncertainty on signal normalization, arising from the assumed amounts of initial and final state radiation.

As detailed above we assign a 50% normalization uncertainty on the multijet prediction, and a 100% uncertainty on the non-collision contamination rate. We propagate the effects of the jet energy scale uncertainty [37] to both the normalization and the shape of the lead-jet E_T for all simulated samples. We incorporate the uncertainty on the shape of the multijet distribution in lead-jet E_T, by forming alternate templates derived from the bin-by-bin difference between the multijet prediction in the Signal Region and the EWK control region. Table V summarizes the systematic uncertainties assumed in the extraction of limits on the dark matter rate.

VI. RESULTS

Event totals are shown in Table VI, with the observed number of events compared to the model prediction for each of the four selections. Model-data comparisons are shown for the $\not\!\!E_T$ and the lead-jet E_T in Figures 3 and 4. In the Signal Region, we do not observe a significant excess over the number of events predicted by our background model, and proceed to quantify the maximum allowed dark matter presence in the data.

We set limits on the dark matter production rate using a Bayesian likelihood [38, 39] formed as a product of likelihoods over bins in the Signal Region lead-jet E_T. We assume a flat prior on the signal rate, and a Gaussian prior for each systematic uncertainty including those affecting sample normalizations and shapes. We set Bayesian 90% credibility level upper limits on $\sigma(p\bar{p} \to \chi\bar{\chi} + \text{jet})$ for each of the 42 model points considered. The expected upper

Contribution	Z	W	diboson	$t\bar{t}$	single-top	multijet	non-collision	Signal
luminosity ($\sigma_{\rm inel}(p\bar{p})$)	3.8	3.8	3.8	3.8	3.8	0	0	3.8
luminosity monitor	4.4	4.4	4.4	4.4	4.4	0	0	4.4
$\lvert Z_0\rvert < 60$ cm efficiency	1	1	1	1	1	0	0	1
non-collision veto over-efficiency	1	1	1	1	1	0	0	1
trigger emulation	2	2	2	2	2	0	0	2
Q^2	2	2	0	0	0	0	0	0
$t\bar{t}$ cross section	0	0	0	10	0	0	0	0
single-top cross section	0	0	0	0	10	0	0	0
diboson cross section	0	0	6	0	0	0	0	0
Z cross section	8	0	0	0	0	0	0	0
W cross section	0	8	0	0	0	0	0	0
initial/final state radiation	0	0	0	0	0	0	0	1.4
p.d.f.	$^{+1.4}_{-1.4}$	$^{+1.4}_{-1.4}$	$^{+0.92}_{-0.62}$	$^{+0.91}_{-1.3}$	$^{+3.1}_{-3.1}$	0	0	$^{+0.93}_{-0.93}$
multijet estimate (shape dep.)	0	0	0	0	0	50	0	0
non-collision normalization	0	0	0	0	0	0	100	0
jet energy scale (shape dep.)	$^{+6}_{-6}$	$^{+8.4}_{-7.9}$	< 0.1	$^{+12.5}_{-14.3}$	$^{+5.8}_{-5.6}$	0	0	$^{+2.8}_{-2.5}$

TABLE V: Summary of systematic uncertainties. Values are percentages.

—— CDF Run II Preliminary 6.7 fb^{-1} ——

Contribution	PreSelection	QCD Control	EWK Control	Signal Region
non-collision	337 ± 337	49 ± 48	1 ± 1	6 ± 6
Z	44636 ± 5393	6949 ± 840	1280 ± 155	22191 ± 2681
W	131070 ± 17552	14986 ± 2007	5582 ± 747	27892 ± 3735
diboson	2843 ± 248	626 ± 55	101 ± 9	412 ± 36
$t\bar{t}$	3887 ± 743	1122 ± 215	20 ± 4	23 ± 4
single-top	2229 ± 303	397 ± 54	27 ± 4	104 ± 14
multijet	280143 ± 140072	165479 ± 82740	1066 ± 533	3278 ± 1639
total background	465145 ± 141799	189608 ± 82787	8076 ± 1011	53904 ± 6022
A-V[$\mathcal{M}_{10\,\rm TeV}, \chi_{1\,\rm GeV}$]@ 50 pb	261 ± 19	52 ± 4	10 ± 1	151 ± 11
data	465084	188361	7942	52633

TABLE VI: Event totals. The dark matter model (A-V[$\mathcal{M}_{10\,\rm TeV}, \chi_{1\,\rm GeV}$]) is axial-vector mediated with 1 GeV dark matter and a mediator mass of 10 TeV. The production rate is set to one pb. Uncertainties are systematic only.

limits at (each model point) are derived by randomly generating 1000 pseudo-datasets (derived from the background prediction), and computing the median of the distribution of resulting upper limits. The upper limits on each model of dark matter production are listed in Tables VII through IX , and shown in Figure 5.

We proceed to convert the limits into constrains on the dark matter-nucleon cross section following [6, 8], and find that our limits compare well to recent direct-detection results. Tables X through XII list the CDF limits on scattering cross sections, while comparisons to several direct-detection results can be seen in Figure 6.

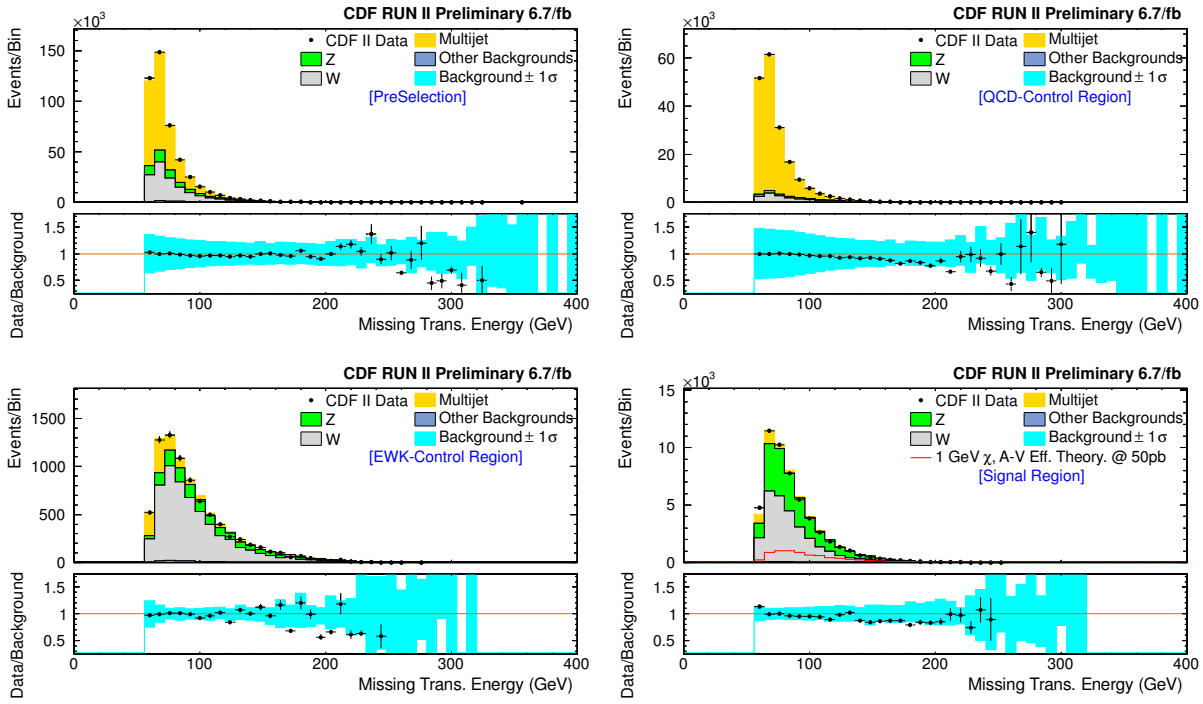

FIG. 3: The $\not\!\!E_T$ in the four selections. The signal shown (lower right) is A-V mediated with 1 GeV dark matter. The mediator mass is 10 TeV.

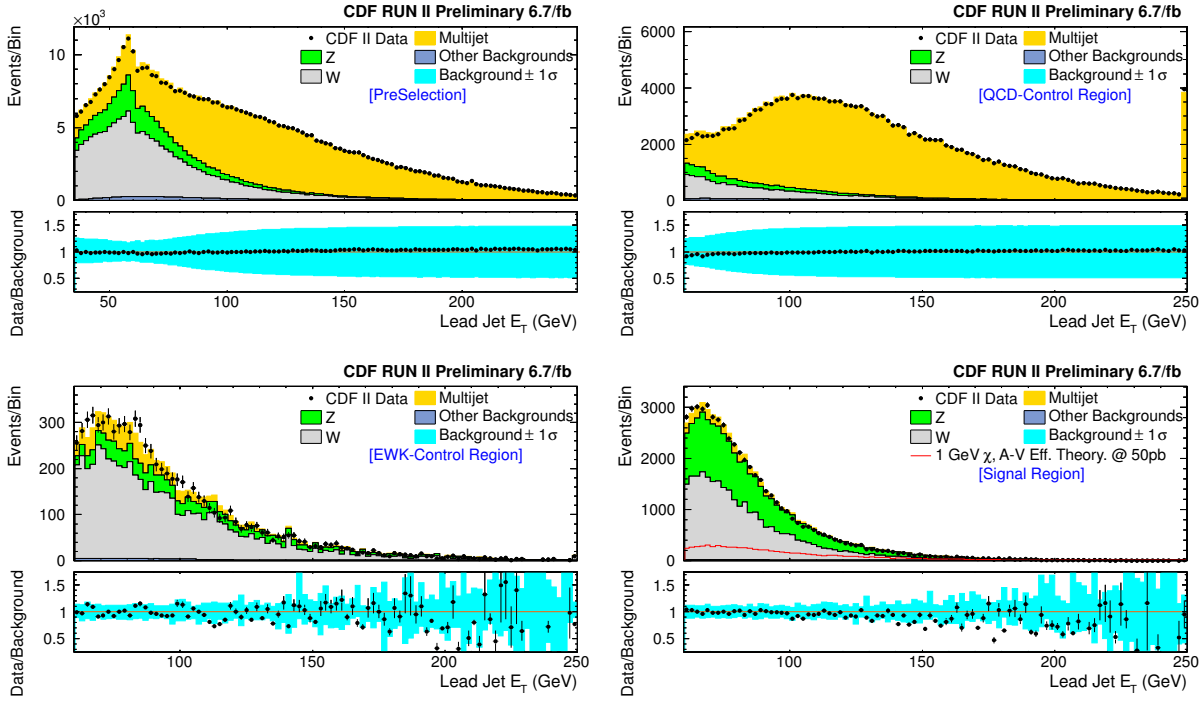

FIG. 4: The lead-jet E_T in the four selections. The signal shown (lower right) is A-V mediated with 1 GeV dark matter. The mediator mass is 10 TeV.

—— Axial-Vector Model 90% CL Upper Limits, CDF Run II Preliminary 6.7 fb^{-1} ——

$M_{\mathcal{M}}$ (GeV)	M_{χ} (GeV)	Observed (pb)	-2σ (pb)	-1σ (pb)	Expected (pb)	$+1\sigma$ (pb)	$+2\sigma$ (pb)
10000	1	5.9	1.8	4.0	7.6	12.5	17.8
10000	5	6.9	1.3	4.3	7.9	12.7	20.0
10000	10	4.5	1.9	4.4	7.9	12.7	19.4
10000	50	3.4	1.3	3.6	7.0	11.2	16.0
10000	100	4.5	1.3	3.1	6.0	9.6	14.4
10000	200	4.8	1.3	2.9	5.6	8.8	13.2
10000	300	3.1	1.2	3.4	6.1	10.0	15.6
100	1	42.8	5.7	13.8	25.6	40.8	61.3
100	5	35.6	4.3	14.1	25.9	41.5	62.1
100	10	31.5	5.5	13.6	23.7	36.6	53.5
100	50	16.0	3.1	9.8	17.8	29.0	42.8
100	100	5.4	1.5	3.6	7.0	11.7	18.6
100	200	3.0	1.1	2.8	5.3	8.7	12.1
100	300	5.6	1.2	2.7	5.2	8.5	13.3

TABLE VII: The 90% CL upper limits on the dark matter production rate in pb. The observed limits are obtained using CDF II data, while the median, -2,-1,+1, and +2 σ values are obtained from the distribution of upper limits obtained in 1000 pseudo-experiments performed at each model point.

—— T-Channel 90% CL Upper Limits, CDF Run II Preliminary 6.7 fb^{-1} ——

$M_{\mathcal{M}}$ (GeV)	M_{χ} (GeV)	Observed (pb)	-2σ (pb)	-1σ (pb)	Expected (pb)	$+1\sigma$ (pb)	$+2\sigma$ (pb)
10000	1	6.5	1.4	3.6	7.2	11.5	17.5
10000	5	7.5	2.1	4.5	8.1	12.5	18.0
10000	10	5.0	1.6	3.9	7.0	11.2	17.3
10000	50	5.3	1.4	3.4	6.5	10.5	16.1
10000	100	4.6	1.4	3.2	6.1	9.8	15.2
10000	200	4.2	1.1	2.6	4.8	8.0	11.9
10000	300	2.7	1.1	2.7	5.1	8.3	12.5
400	1	1.6	0.5	0.8	1.3	2.1	3.2
400	5	1.4	0.5	0.8	1.3	2.1	3.3
400	10	1.4	0.4	0.8	1.3	2.2	3.5
400	50	1.0	0.4	0.8	1.3	2.1	3.2
400	100	1.0	0.4	0.8	1.3	2.1	3.2
400	200	1.1	0.6	1.1	2.0	3.2	4.9
400	300	3.9	0.9	2.5	4.6	7.5	11.4

TABLE VIII: The 90% CL upper limits on the dark matter production rate in pb. The observed limits are obtained using CDF II data, while the median, -2,-1,+1, and +2 σ values are obtained from the distribution of upper limits obtained in 1000 pseudo-experiments performed at each model point.

—— Vector Model 90% CL Upper Limits, CDF Run II Preliminary 6.7 fb^{-1} ——

$M_{\mathcal{M}}$ (GeV)	M_{χ} (GeV)	Observed (pb)	-2σ (pb)	-1σ (pb)	Expected (pb)	$+1\sigma$ (pb)	$+2\sigma$ (pb)
10000	1	9.1	1.7	4.3	7.8	12.8	19.5
10000	5	5.4	1.5	4.0	8.1	13.0	19.7
10000	10	6.4	1.5	4.1	7.7	12.1	18.4
10000	50	6.6	1.3	4.1	7.5	12.1	19.7
10000	100	5.7	1.2	3.4	6.2	9.9	14.5
10000	200	3.9	1.3	2.9	5.6	9.2	14.1
10000	300	3.5	1.3	3.2	5.6	9.0	13.3
100	1	18.9	4.4	14.0	26.6	42.3	64.4
100	5	36.4	4.1	13.2	23.4	36.6	54.5
100	10	25.2	4.5	14.1	25.2	39.5	59.6
100	50	20.9	4.6	11.9	21.0	33.7	49.4
100	100	5.1	1.8	4.2	8.4	13.7	19.6
100	200	5.3	1.4	3.1	5.6	9.0	13.3
100	300	4.6	1.1	2.8	5.5	9.0	14.2

TABLE IX: The 90% CL upper limits on the dark matter production rate in pb. The observed limits are obtained using CDF II data, while the median, -2,-1,+1, and +2 σ values are obtained from the distribution of upper limits obtained in 1000 pseudo-experiments performed at each model point.

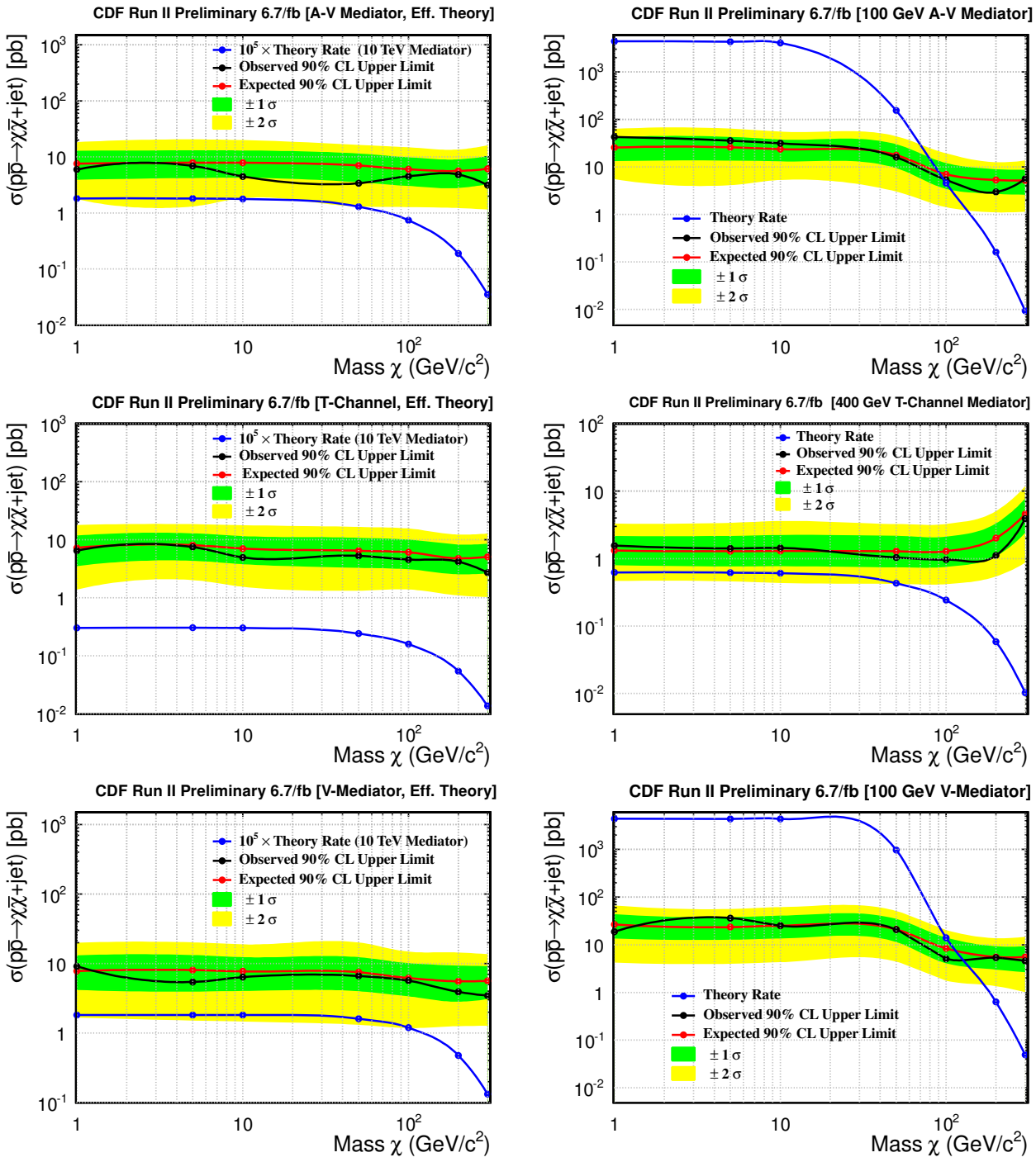

FIG. 5: The 90% CL upper limits on the dark matter production rate in pb for models with heavy mediators. The observed limits are obtained using CDF II data, while the median, -2,-1,+1, and +2 σ values are obtained from the distribution of upper limits obtained in 1000 pseudo-experiments performed at each model point.

Axial-Vector Model 90% CL Upper Limits on σ_{SD-p}, CDF Run II Preliminary 6.7 fb^{-1}

$M_{\mathcal{M}}$ (GeV)	M_{χ} (GeV)	Observed (cm^2)	-2σ (cm^2)	-1σ (cm^2)	Expected (cm^2)	$+1\sigma$ (cm^2)	$+2\sigma$ (cm^2)
10000	1	3.1e-40	9.5e-41	2.1e-40	4.0e-40	6.6e-40	9.3e-40
10000	5	9.6e-40	1.9e-40	6.0e-40	1.1e-39	1.8e-39	2.8e-39
10000	10	7.5e-40	3.2e-40	7.4e-40	1.3e-39	2.1e-39	3.3e-39
10000	50	9.0e-40	3.6e-40	9.7e-40	1.9e-39	3.0e-39	4.2e-39
10000	100	2.1e-39	6.1e-40	1.5e-39	2.8e-39	4.5e-39	6.8e-39
10000	200	9.1e-39	2.4e-39	5.4e-39	1.1e-38	1.6e-38	2.5e-38
10000	300	3.1e-38	1.2e-38	3.4e-38	6.2e-38	1.0e-37	1.6e-37
100	1	9.2e-40	1.2e-40	3.0e-40	5.5e-40	8.8e-40	1.3e-39
100	5	2.1e-39	2.5e-40	8.2e-40	1.5e-39	2.4e-39	3.6e-39
100	10	2.3e-39	4.0e-40	9.8e-40	1.7e-39	2.7e-39	3.9e-39
100	50	3.6e-38	7.0e-39	2.2e-38	3.9e-38	6.4e-38	9.5e-38
100	100	4.1e-37	1.1e-37	2.7e-37	5.4e-37	8.9e-37	1.4e-36
100	200	6.5e-36	2.5e-36	6.2e-36	1.2e-35	1.9e-35	2.7e-35
100	300	2.1e-34	4.5e-35	1.0e-34	1.9e-34	3.2e-34	5.0e-34

TABLE X: The 90% CL upper limits on the spin-dependent dark matter-nucleon scattering cross section in cm^2. The observed limits are obtained using CDF II data, while the median, -2,-1,+1, and +2 σ values are obtained from the distribution of upper limits obtained in 1000 pseudo-experiments performed at each model point.

VII. CONCLUSIONS

In conclusion we have performed a search for dark matter in the monojet + $\not\!\!E_T$ signature and have found the data to be in agreement with the background-only expectation. We have produced 90% credibility level upper limits on 42 model points with varied values of mediator and dark matter mass between 0.96 and 42.8 pb. We have translated our limits into bounds on the dark matter nucleon scattering rate for both spin-dependent (σ_{SD-p}) and spin-independent (σ_{SI-p}) interactions, and find them to be competitive with direct-detection searches.

t-channel Model 90% CL Upper Limits on σ_{SI-p}, CDF Run II Preliminary 6.7 fb^{-1}

$M_{\mathcal{M}}$ (GeV)	M_{χ} (GeV)	Observed (cm^2)	-2σ (cm^2)	-1σ (cm^2)	Expected (cm^2)	$+1\sigma$ (cm^2)	$+2\sigma$ (cm^2)
10000	1	3.5e-39	7.6e-40	1.9e-39	3.9e-39	6.2e-39	9.4e-39
10000	5	1.1e-38	3.0e-39	6.4e-39	1.2e-38	1.8e-38	2.6e-38
10000	10	8.4e-39	2.7e-39	6.6e-39	1.2e-38	1.9e-38	2.9e-38
10000	50	1.3e-38	3.3e-39	8.3e-39	1.6e-38	2.6e-38	4.0e-38
10000	100	1.7e-38	5.4e-39	1.2e-38	2.3e-38	3.7e-38	5.7e-38
10000	200	4.7e-38	1.3e-38	2.9e-38	5.4e-38	8.9e-38	1.3e-37
10000	300	1.2e-37	4.7e-38	1.2e-37	2.3e-37	3.7e-37	5.5e-37
400	1	1.6e-39	4.9e-40	8.4e-40	1.3e-39	2.2e-39	3.3e-39
400	5	3.9e-39	1.3e-39	2.1e-39	3.5e-39	5.8e-39	9.1e-39
400	10	4.7e-39	1.5e-39	2.6e-39	4.3e-39	7.2e-39	1.2e-38
400	50	5.5e-39	2.3e-39	4.1e-39	6.9e-39	1.1e-38	1.7e-38
400	100	9.3e-39	4.2e-39	7.5e-39	1.2e-38	2.0e-38	3.1e-38
400	200	4.5e-38	2.3e-38	4.5e-38	8.1e-38	1.3e-37	2.0e-37
400	300	9.0e-37	2.1e-37	5.8e-37	1.1e-36	1.7e-36	2.6e-36

TABLE XI: The 90% CL upper limits on the spin-independent dark matter-nucleon scattering cross section in cm^2. The observed limits are obtained using CDF II data, while the median, -2,-1,+1, and +2 σ values are obtained from the distribution of upper limits obtained in 1000 pseudo-experiments performed at each model point.

Vector Model 90% CL Upper Limits on σ_{SI-p}, CDF Run II Preliminary 6.7 fb^{-1}

$M_{\mathcal{M}}$ (GeV)	M_{χ} (GeV)	Observed (cm^2)	-2σ (cm^2)	-1σ (cm^2)	Expected (cm^2)	$+1\sigma$ (cm^2)	$+2\sigma$ (cm^2)
10000	1	1.3e-38	2.5e-39	6.1e-39	1.1e-38	1.9e-38	2.8e-38
10000	5	2.1e-38	5.9e-39	1.5e-38	3.1e-38	5.0e-38	7.5e-38
10000	10	2.9e-38	6.7e-39	1.9e-38	3.5e-38	5.4e-38	8.3e-38
10000	50	3.9e-38	7.9e-39	2.4e-38	4.4e-38	7.1e-38	1.2e-37
10000	100	4.6e-38	9.8e-39	2.8e-38	5.0e-38	8.0e-38	1.2e-37
10000	200	8.0e-38	2.6e-38	5.9e-38	1.1e-37	1.9e-37	2.9e-37
10000	300	2.5e-37	9.6e-38	2.3e-37	4.2e-37	6.7e-37	9.8e-37
100	1	1.1e-38	2.6e-39	8.3e-39	1.6e-38	2.5e-38	3.8e-38
100	5	5.8e-38	6.5e-39	2.1e-38	3.7e-38	5.8e-38	8.6e-38
100	10	4.7e-38	8.3e-39	2.6e-38	4.7e-38	7.4e-38	1.1e-37
100	50	2.0e-37	4.4e-38	1.1e-37	2.0e-37	3.3e-37	4.8e-37
100	100	3.5e-36	1.2e-36	2.9e-36	5.8e-36	9.4e-36	1.3e-35
100	200	8.2e-35	2.1e-35	4.8e-35	8.5e-35	1.4e-34	2.0e-34
100	300	9.1e-34	2.1e-34	5.5e-34	1.1e-33	1.8e-33	2.8e-33

TABLE XII: The 90% CL upper limits on the spin-independent dark matter-nucleon scattering cross section in cm^2. The observed limits are obtained using CDF II data, while the median, -2,-1,+1, and +2 σ values are obtained from the distribution of upper limits obtained in 1000 pseudo-experiments performed at each model point.

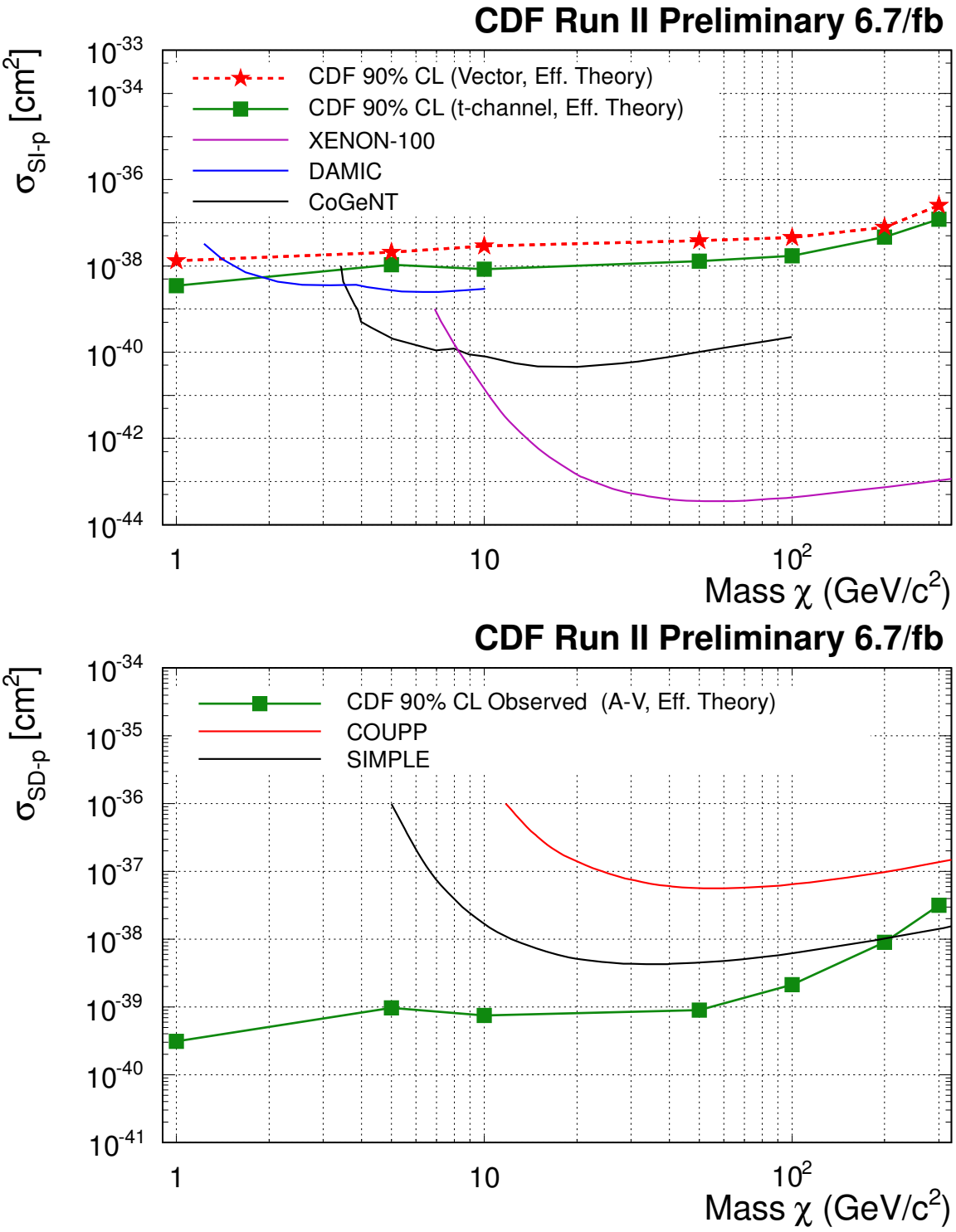

FIG. 6: Comparison of CDF results with heavy mediators to recent results from COUPP [40], SIMPLE [41], XENON-100 [42], DAMIC [43], and CoGeNT [44]. Spin-independent (σ_{SI-p}) bounds are shown in the upper figure, while the lower figure displays spin-dependent (σ_{SD-p}) limits.

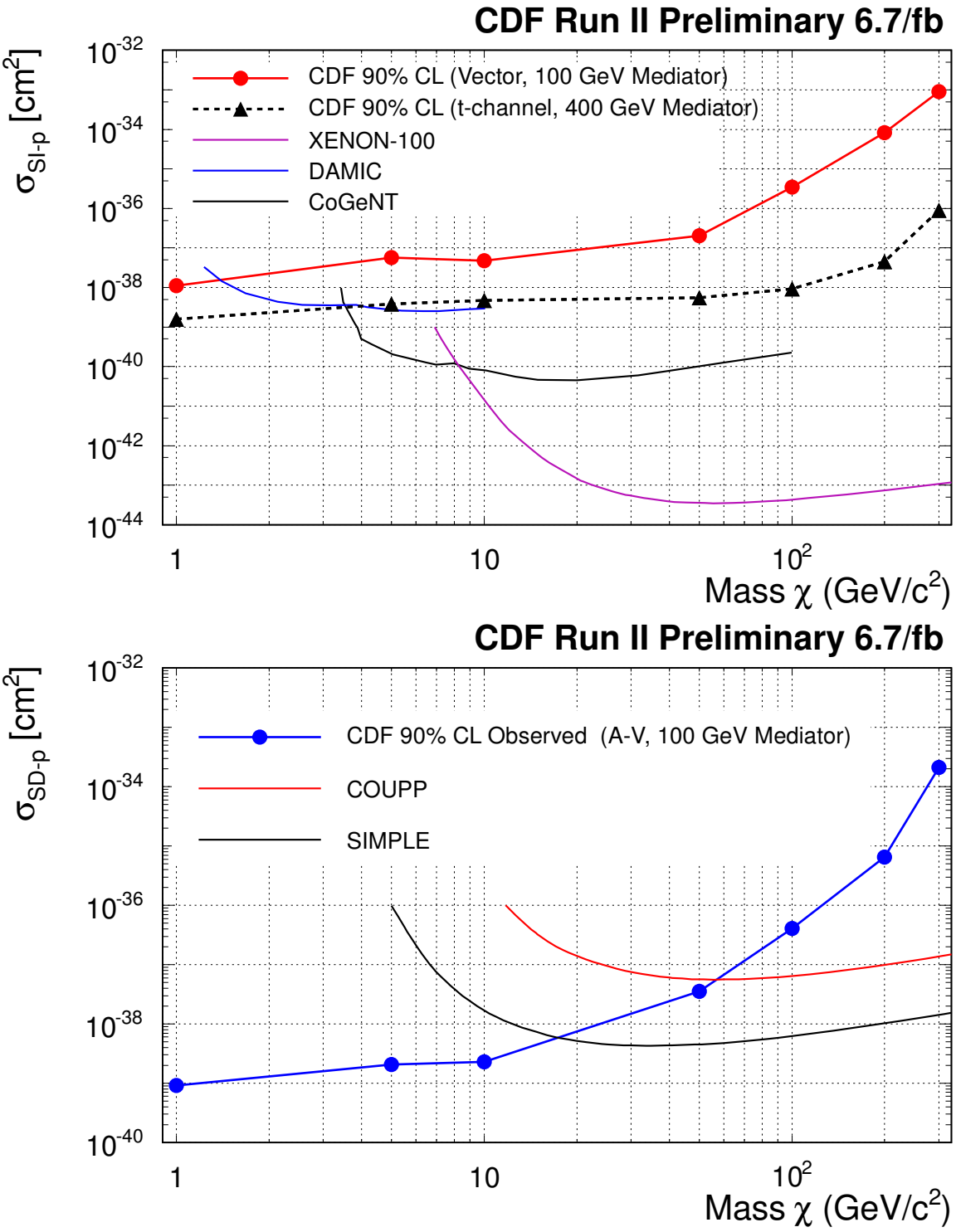

FIG. 7: Comparison of CDF results with light mediators to recent results from COUPP [40], SIMPLE [41], XENON-100 [42], DAMIC [43], and CoGeNT [44]. Spin-independent (σ_{SI-p}) bounds are shown in the upper figure, while the lower figure displays spin-dependent (σ_{SD-p}) limits.

[1] K. Garrett and G. Duda, Adv. Astron. **2011**, 968283 (2011), hep-ph/1006.2483.
[2] D. B. Cline (2011), astro-ph.CO/1109.1799.
[3] R. Bernabei et al., Eur. Phys. J. **C67**, 39 (2010), astro-ph.GA/1002.1028.
[4] C. E. Aalseth et al. (CoGeNT), Phys. Rev. Lett. **106**, 131301 (2011), astro-ph.CO/1002.4703.
[5] G. Angloher et al. (2011), astro-ph.CO/1109.0702.
[6] Y. Bai, P. J. Fox, and R. Harnik, JHEP **12**, 048 (2010), 1005.3797.
[7] P. J. Fox, R. Harnik, J. Kopp, and Y. Tsai (2011), hep-ph/1109.4398.
[8] J. Goodman et al., Phys. Lett. **B695**, 185 (2011), hep-ph/1005.1286.
[9] J. Goodman et al., Phys. Rev. **D82**, 116010 (2010), hep-ph/1008.1783.
[10] T. Aaltonen et al. (CDF), Phys. Rev. Lett. **101**, 181602 (2008), hep-ex/0807.3132.
[11] S. A. Malik (2011), hep-ex/1110.1609.
[12] G. Aad et al. (ATLAS), Phys. Lett. **B705**, 294 (2011), hep-ex/1106.5327.
[13] F. Maltoni and T. Stelzer, JHEP **02**, 027 (2003), hep-ph/0208156.
[14] P. J. Fox, R. Harnik, J. Kopp, and Y. Tsai, Phys. Rev. **D84**, 014028 (2011), 1103.0240.
[15] We use a cylindrical coordinate system with z along the proton beam direction, r the perpendicular radius from the central axis of the detector, and ϕ the azimuthal angle. For θ the polar angle from the proton beam, we define $\eta = -\ln\tan(\theta/2)$, transverse momentum $p_T = p\sin\theta$ and transverse energy $E_T = E\sin\theta$.
[16] The effects of varying the widths have been studied in [7, 14].
[17] The missing E_T ($\vec{\not\!\!E}_T$) is defined by the sum over calorimeter towers: $\vec{\not\!\!E}_T = -\sum_i E_T^i \hat{n}_i$, where i = calorimeter tower number with $|\eta| < 3.6$, $\hat{n}_i$ is a unit vector perpendicular to the beam axis and pointing at the ith calorimeter tower. We also define $\not\!\!E_T = |\vec{\not\!\!E}_T|$.
[18] D. Acosta et al. (CDF Collaboration), Phys. Rev. D **71**, 052003 (2005).
[19] We consider only tracks with $p_T > 10$ GeV/c. An isolated track contributes dominantly to the sum of the transverse momentum of all objects contained within a radius of 0.1 (in $\eta - \phi$) centered around the track.
[20] We require the primary interaction vertex of the event to be within $|Z_0| < 60$ cm of the detector center.
[21] We define jets using a cone size of 0.4, and apply 'L5' corrections. We do not consider jets with $E_T < 20$ GeV or with detector $|\eta| > 2.4$.
[22] CDF Internal Note 6100 (2002) [restricted document].
[23] We define the event emfraction as $\frac{\sum_i E_T^i \times EmFrac_i}{\sum_i E_T^i}$ where i runs over all jets with $E_T > 20$ GeV and detector $|\eta| \leq 2.4$, and $EmFrac_i$ is the ratio of the electro-magnetic to hadronic energies of the i^{th} jet.
[24] We define the $\not\!\!E_T$ significance as $\frac{\not\!\!E_T}{\sum_i E_T^i}$ where i runs over all jets with $E_T > 20$ GeV and detector $|\eta| \leq 2.4$.
[25] We define the event trkMET$_{10}$ as $-1 \times \sum_i \vec{p_T}_i$ where i runs over all tracks with $p_T > 10$ GeV/c.
[26] http://tmva.sourceforge.net.
[27] We define R = (scalar sum of lead and sub-leading jet E_T's) / (scalar sum of lead and sub-leading jet E_T's and $\not\!\!E_T$).
[28] M. L. Mangano et al., J. High Energy Phys. **07**, 001 (2003).
[29] T. Sjöstrand *et al.*, Comput. Phys. Comm. **135**, 238 (2001). We use "Pythia Tune A", R. Field and R. C. Group, hep-ph/0510198v1.
[30] R. Brun et al., *GEANT 3: User's Guide Geant 3.10, Geant 3.11; rev. version* (CERN, Geneva, 1987).
[31] CDF Internal Note 10474 (2011) [restricted document].
[32] H. L. Lai et al. (CTEQ), Eur. Phys. J. **C12**, 375 (2000), hep-ph/9903282.
[33] The parameterization is determined in a sample of events containing high-p$_T$ muons.
[34] CDF Internal Note 9261 (2009) [restricted document].
[35] A. Abulencia et al. (CDF), J. Phys. **G34**, 2457 (2007), hep-ex/0508029.
[36] http://www-cdf.fnal.gov/internal/physics/joint_physics/instructions/PDFUncertainties/pdf.html.
[37] A. Bhatti et al., Nucl. Instrum. Methods Phys. Res., Sect. A **566**, 375 (2006).
[38] CDF Internal Note 7587 (2005) [restricted document].
[39] CDF Internal Note 8128 (2006) [restricted document].
[40] E. Behnke et al., Phys. Rev. Lett. **106**, 021303 (2011), astro-ph.CO/1008.3518.
[41] M. Felizardo et al. (2011), astro-ph.CO/1106.3014.
[42] E. Aprile et al. (XENON100), Phys. Rev. Lett. **105**, 131302 (2010), astro-ph.CO/1005.0380.
[43] J. Barreto et al. (DAMIC) (2011), astro-ph.IM/1105.5191.
[44] C. E. Aalseth et al. (CoGeNT), Phys. Rev. Lett. **106**, 131301 (2011), astro-ph.CO/1002.4703.